

Article

Spatial and Temporal Variations of Atmospheric CO₂ Concentration in China and Its Influencing Factors

Zhenghan Lv ^{1,2} , Yusheng Shi ^{2,*} , Shuying Zang ^{1,*} and Li Sun ¹

¹ Heilongjiang Province Key Laboratory of Geographical Environment Monitoring and Spatial Information Service in Cold Regions, Harbin Normal University, Harbin 150025, China; hanlzh@outlook.com (Z.L.); sunli_wabb@163.com (L.S.)

² State Environmental Protection Key Laboratory of Satellite Remote Sensing, Aerospace Information Research Institute, Chinese Academy of Sciences, Beijing 100101, China

* Correspondence: shiys@aircas.ac.cn (Y.S.); zsy6311@hrbnu.edu.cn (S.Z.)

Received: 1 February 2020; Accepted: 25 February 2020; Published: 27 February 2020



Abstract: Over the past few decades, concentrations of carbon dioxide (CO₂), a key greenhouse gas, have risen at a global rate of approximately 2 ppm/a. China is the largest CO₂ emitter and is the principle contributor to the increase in global CO₂ levels. Based on a satellite-retrieved atmospheric carbon dioxide column average dry air mixing ratio (XCO₂) dataset, derived from the greenhouse gas observation satellite (GOSAT), this paper evaluates the spatial and temporal variations of XCO₂ characteristics in China during 2009–2016. Moreover, the factors influencing changes in XCO₂ were investigated. Results showed XCO₂ concentrations in China increased at an average rate of 2.28 ppm/a, with significant annual seasonal variations of 6.78 ppm. The rate of change of XCO₂ was greater in south China compared to other regions across China, with clear differences in seasonality. Seasonal variations in XCO₂ concentrations across China were generally controlled by vegetation dynamics, characterized by the Normalized Difference Vegetation Index (NDVI). However, driving factors exhibited spatial variations. In particular, a distinct belt (northeast–southwest) with a significant negative correlation ($r < -0.75$) between XCO₂ and NDVI was observed. Furthermore, in north China, human emissions were identified as the dominant influencing factor of total XCO₂ variations ($r > 0.65$), with forest fires taking first place in southwest China ($r > 0.47$). Our results in this study can provide us with a potential way to better understand the spatiotemporal changes of CO₂ concentration in China with NDVI, human activity and biomass burning, and could have an enlightening effect on slowing the growth of CO₂ concentration in China.

Keywords: carbon dioxide (CO₂); GOSAT; spatial variation; temporal trends; influencing factors

1. Introduction

Atmospheric carbon dioxide (CO₂) is an important element of the global carbon cycle and a major greenhouse gas due to its extensive contributes to global warming. CO₂ concentrations have increased by more than 40% since the Industrial Revolution [1]. In addition, a warmer climate with adverse consequences, such as rising sea levels and an increase in extreme weather conditions, mean that further increases in CO₂ levels are expected [2]. More specifically, according to the National Oceanic and Atmospheric Administration (NOAA), the global CO₂ concentration increased from 368.84 ppm in 2000 to 402.86 ppm in 2016, with an average growth rate of 2.06 ppm/a [3]. Since 2006, China has been the world's largest emitter of CO₂ [4,5]. The annual growth rate of atmospheric XCO₂ concentration reached 2.16 ppm/a in China, and the monthly average concentration of CO₂ exceeded the global average by 1.63 ppm during 2006–2016. For example, in 2016, China released approximately 1.02×10^4 Mt CO₂ into the atmosphere, contributing to 28% of total global carbon

emissions [6]. Furthermore, CO₂ emissions in China exceeded the total emissions of the United States, the European Union and Japan in 2016 [6]. Therefore, the CO₂ emissions in China have a significant impact on global atmospheric CO₂ concentrations.

Traditionally, the monitoring of atmospheric CO₂ concentrations generally relies on measurements from ground stations distributed across the globe [7–9]. However, the development of satellite remote sensing technology allows for the real-time observation and mapping of the spatial and temporal distribution of global atmospheric CO₂ concentrations [10,11]. For example, the widely used SCanning Imaging Absorption SpectroMeter for Atmospheric CHartographY (SCIAMACHY) datasets, developed by the European Space Agency (ESA), provide global spatial and temporal distributions of atmospheric trace gas concentrations, and are commonly used in global carbon source/sink simulations and atmospheric transport models [12–14]. Satellite observations effectively increase the breadth of observation data and save time costs. Therefore, satellite remote sensing inversion has become the dominant quantitative observation approach for atmospheric greenhouse gases [15–18].

The world's first greenhouse gas observation satellite (GOSAT), launched in 2009 by the Japan Aerospace Exploration Agency (JAXA), the National Institute for Environmental Studies (NIES) and the Ministry of the Environment (MOE), is specifically designed to record atmospheric greenhouse gas column average dry air mixing ratios (XCO₂ and XCH₄) [19–21]. The GOSAT satellite uses solar radiation in the near-infrared/shortwave-infrared (NIR/SWIR) regions and variations in the thermal infrared (TIR) bands [22,23] to determine the target mixing ratios. In particular, SWIR observations are sensitive to the CO₂ abundance from the surface to the top of the troposphere, while TIR observations are sensitive to CO₂ in the upper and middle troposphere, particularly the CO₂ concentration profile [24,25]. GOSAT provides global coverage and multi-year datasets that have been used in multiple applications, including atmospheric simulations, ecosystem flux retrievals and regional environmental quality assessments [26–29]. Furthermore, GOSAT provides a large number of atmospheric data products, including XCO₂ concentration data, which allows for the determination of spatial and temporal trends in global atmospheric XCO₂ concentrations, as well as atmospheric XCO₂ concentration variations and potential carbon source–sink distributions [30–32]. Some scholars have done meaningful related research in this regard [25,29,33]. However, the study periods or spatial scales are limited [34,35]. In addition, most scholars focus their research on accuracy/uncertainty analysis [5,36,37], and some studies compared the difference of CO₂ concentration in the same area from different satellites [31,37] or investigated the effect of a single carbon source/sink on the concentration of CO₂; for example, the studies of CO₂ emissions from anthropogenic activities [32,38], the impact of vegetable absorption [14,39] and the estimated CO₂ emissions from forest fires [10,40]. However, these studies lack comprehensive consideration of multiple factors.

As a major greenhouse gas emitter, long-term serial observations of atmospheric CO₂ concentrations in China have become very important. Spatial and temporal distribution differences based on long-term sequence changes can help us to understand the underlying characteristics of atmospheric XCO₂ concentration changes in China. In this study, we interpolated GOSAT Level-2 CO₂ data from 2009 to 2016 to obtain a monthly CO₂ concentration dataset in China. Then, based on the results of its changing characteristics, the three main influencing factors of vegetation, anthropogenic activities and biomass burning are combined to explain the changing characteristics of atmospheric CO₂ concentration in mainland China. The current study aims to investigate the spatial and temporal characteristics of XCO₂ concentrations and the influencing factors of XCO₂ variations in China during 2009–2016. Our results in this study can provide us with a potential way to better understand how the spatiotemporal changes of CO₂ concentration in China with NDVI, human activity and biomass burning. It could also have an enlightening effect on slowing the growth of CO₂ concentration in China.

2. Data and Methods

2.1. Data

2.1.1. CO₂ Data

The GOSAT satellite was successfully launched by JAXA with a sun-synchronous orbit in Japan 2009. It has a spatial resolution of 10.5 km × 10.5 km, transits at 13:00 local time and has a replay period of 3 days [41,42]. There are two main sensors in the GOSAT, the Fourier Transform Spectrometer (FTS) and the Cloud Aerosol Imager (CAI), measuring atmospheric greenhouse gases, clouds and radiation, respectively. The FTS sensor can observe the average column concentration distribution of CO₂ and CH₄ by analyzing the atmospheric gas composition derived from spectral information of the atmosphere. GOSAT data products are widely used in the detection of fire emissions and human activity [43–45].

We selected monthly data from TANSO FTS SWIR based on the NIES Level-2 V02.72 algorithm during April 2009 to December 2016. However, due to the observation orbit of GOSAT, data was unavailable for each pan-winter (November to March), resulting in a large number of missing values for high latitudes across the globe. Therefore, we analyzed two conditions of the whole year, as well as the vegetation growing season during 2009–2016. Furthermore, we compared the corresponding satellite data with site observation datasets from atmospheric background stations (Mt. Waliguan (WLG) Station (100.9° N, 36.28° E) and Mt. Lulin (LL) Station (23.47° N, 120.84° E)) in China, in order to verify the accuracy of the GOSAT data. The site observation datasets were obtained from the National Oceanic and Atmospheric Administration Earth System Research Laboratory (NOAA/ESRL) in the World Greenhouse Gas Data Center (WDCGG) from 2009 to 2016.

2.1.2. Ancillary Data

(1) Normalized Difference Vegetation Index (NDVI).

NDVI quantifies vegetation by measuring the difference between the near-infrared and red regions of the electromagnetic spectrum, which can indicate the state of vegetation growth and dynamics over time. Vegetation is able to reduce atmospheric CO₂ concentrations via photosynthesis. NDVI values close to 1 (0) denote vigorous (sparse) vegetation growth. Hence, NDVI indirectly indicates the photosynthetic capacity of vegetation, which has a strong impact on atmospheric CO₂ concentrations [43,46]. Therefore, we used monthly Moderate-resolution Imaging Spectroradiometer (MODIS) NDVI Level-3 data from EOS (NASA) to represent the carbon sink.

(2) Open-Source Data Inventory for Anthropogenic CO₂ (ODIAC).

ODIAC is a 1 × 1 km monthly global high-resolution gridded fossil fuel CO₂ emissions data product (unit: g CO₂/m²/d) [47]. It can effectively represent the amount of CO₂ emitted by human activity to the atmosphere on a monthly basis and includes emissions from thermal power generation and cement manufacturing. Fossil fuel CO₂ emission datasets from 2000 to 2017 was selected in this study.

(3) Global Fire Emissions Database v4.1s (GFEDv4.1s).

GFED quantifies global trace gases and aerosol emissions from global biomass burning [48]. The CO₂ emissions from biomass burning are determined via satellite-retrieved burned area, biogeochemical model-simulated fuel loads, moisture-regulated combustion factors, and land cover-based emission factors (unit: g CO₂/m²/month) [49]. The latest version of GFED (v4.1s) includes small fire emissions that were missed in previous datasets, as well as daily resolution updates. In the current study, we derived the monthly fire CO₂ emissions from different types of biomass burning with a 0.25° × 0.25° grid size from 2009 to 2016. These were subsequently linearly resampled to a 0.1° × 0.1° grid size for consistency with the above datasets.

2.2. Statistical Analysis Methods

2.2.1. Standard Deviation Ellipse Analysis

Standard deviation ellipse (SDE) analysis is commonly used to analyze spatial distribution directional characteristics with time. The size of the ellipse reflects the concentration of the overall elements of the spatial pattern, while the declination (long semi-axis) reflects the dominant direction of the spatial pattern. Using years of standard deviation statistics enables us to understand average center, major/minor axes and azimuths trends of the discrete point set in time series [50,51]. Therefore, the standard deviation ellipse can express the main distribution direction of a set of points and the degree of dispersion in all directions. These two factors are usually used to describe the overall characteristics of a geospatial distribution [51]. In the current study, we applied SDE analysis results of the annual mean XCO₂ concentrations in China from 2009 to 2016. By plotting the abstract images of the elliptical motion trajectories of China's annual average XCO₂ concentration, the dynamic changes of these ellipses over time are obtained, which cannot be demonstrated using a pixel-level analysis. Therefore, we used an SDE analysis of the annual mean XCO₂ concentrations in China from 2009 to 2016.

2.2.2. Pixel-Based Time Series Analysis

In order to investigate the interannual variability of the local spatial non-stationarity of atmospheric XCO₂ concentrations over 2009–2016, we used the linear long-term trend (LLT) to quantitatively analyze long-sequence XCO₂ concentration images during the growing season. By using LLT, we can comprehensively understand the spatial and temporal changes in atmospheric XCO₂ concentrations. The time series of monthly atmospheric XCO₂ concentration data was fitted by pixel-by-pixel linear regression. The LLT slope represents XCO₂ concentration change trends (k), as it embodies the direction and magnitude of XCO₂ changes across time. More specifically, positive (negative) slopes denote increases (decreases) in the XCO₂ concentration in the specific pixel, while for slopes close to zero, the pixel is identified as “stable”. The LLT slope was calculated as follows:

$$k = \frac{n \times \sum_{i=1}^n (i \times XCO_{2i}) - (\sum_{i=1}^n i)(\sum_{i=1}^n XCO_{2i})}{n \times \sum_{i=1}^n i^2 - (\sum_{i=1}^n i)^2} \quad (1)$$

where XCO₂ is the grid unit XCO₂ concentration, n is the time span and i is the time unit.

3. Results

Figure 1 presents the derived multi-year average atmospheric XCO₂ concentrations in most part of China, with high latitudes masked due to absent values in winter. Spatial variations were observed in the eastern and western regions of China, with concentrations gradually decreasing from east to west. The maximum concentration (395.50 ppm) was observed in Shanghai, located in the coastal area of east China, with the lower atmospheric XCO₂ concentrations (less than 393.00 ppm) observed over the Tibetan Plateau.

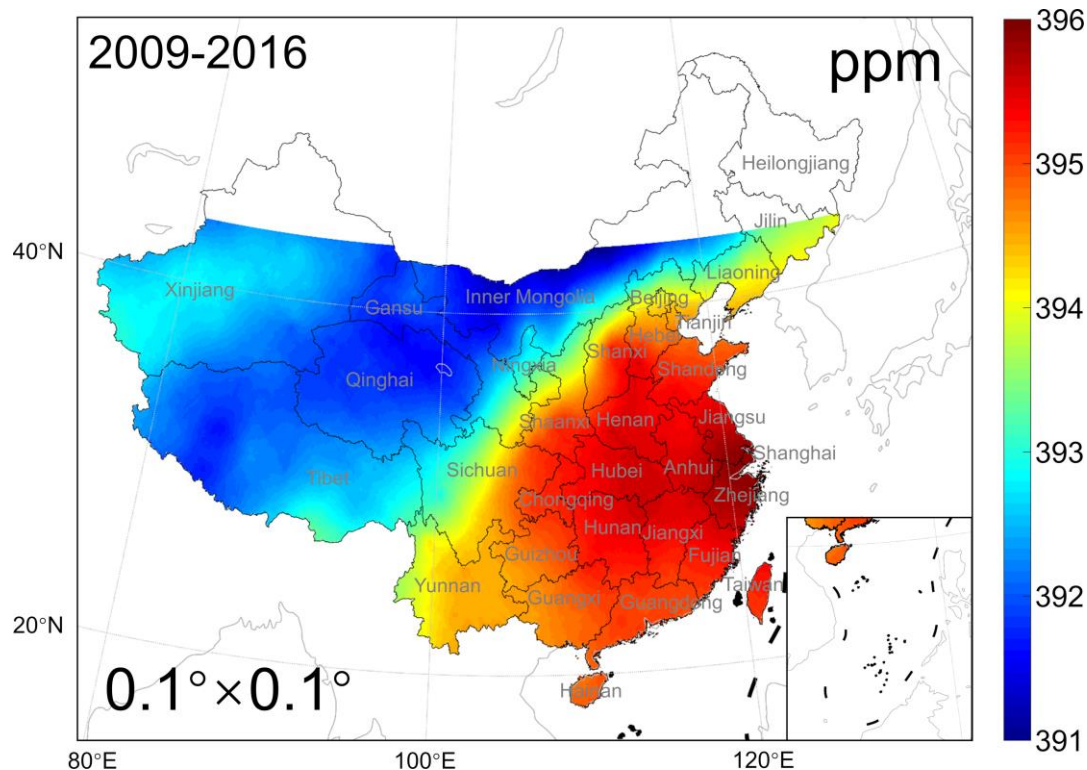


Figure 1. Average concentrations of atmospheric XCO₂ (ppm) during 2009–2016.

3.1. Validation of XCO₂ Concentrations via *in situ* Data

In order to assess the accuracy of GOSAT data, we compared the satellite-derived XCO₂ data with that measured from the WLG and LL stations (Figure 2). The atmospheric environment and components of the WLG station were relatively stable, due to its distance from built-up areas. There was a good agreement between the two datasets, ($r = 0.94$, RMSE = 2.2 ppm). Similarly, to the WLG station, the LL station is located in the mountains, yet it is influenced by a tropical–subtropical monsoon climate and marine atmospheric environment. The measured CO₂ variation range of the LL station is larger than that of the WLG station during 2009–2016 ($r = 0.95$, RMSE = 2.5 ppm).

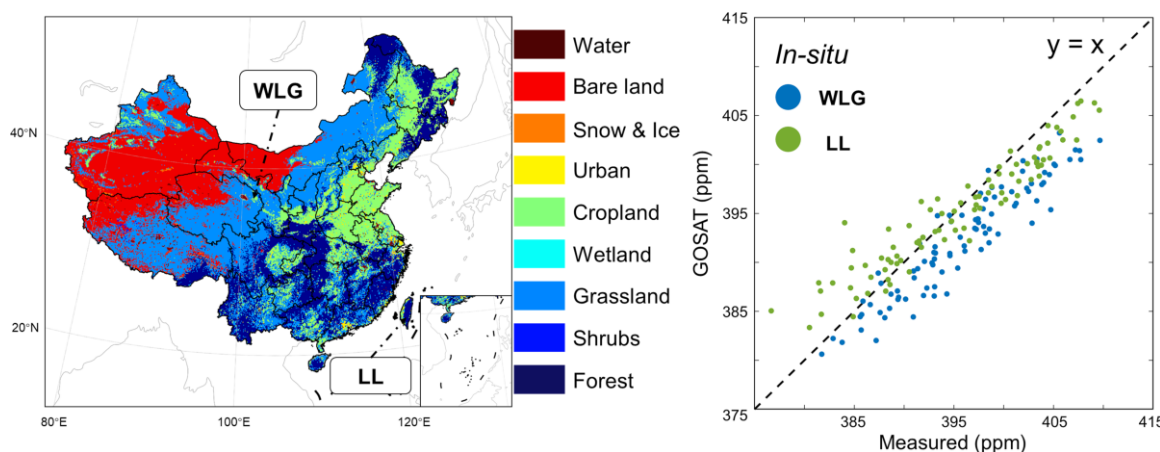


Figure 2. Locations of the Mt. Waliguan station (WLG) and Mt. LuLin station (LL) in China and the comparison with GOSAT.

Furthermore, based on the derived statistics of each site, the XCO₂ concentrations were lower than those from the measured ground data by 0.88% (WLG) and 0.05% (LL), respectively (Table 1). In addition, the WLG station showed more accurate verification results, followed by the LL station. This is attributed to the different measurement scales. More specifically, the station-measured dataset is made up of surface point data, while the GOSAT XCO₂ data compromises regional tropospheric column averages at a spatial resolution of 10.5 km × 10.5 km. This observation is similar to Guo et al. (2015), who used MODIS and GOSAT L2 data to model XCO₂ concentrations during the 2012–2013 growing seasons and determined an average bias of 2.25 ppm [33]. This indicates that the monthly XCO₂ data obtained by interpolation is relatively reliable and can be used for subsequent analysis.

Table 1. Comparison between GOSAT satellite observations and ground measurements.

Stations	Sample Number	Mean(ppm)		Std(ppm)		Correlation Coefficient	RMSE (ppm)
		Measured	GOSAT	Measured	GOSAT		
Mt. WLG	92	395.9	392.4	6.4	5.5	0.94	2.2
Mt. Lulin	90	395.3	395.1	7.8	5.7	0.95	2.5

3.2. Seasonal XCO₂ Variations

The temporal characteristics of atmospheric tropospheric XCO₂ concentrations in China exhibited strong seasonal variations and rising trends (Figure 3). The XCO₂ concentrations rose from 387.24 ppm in April 2009 to 404.09 ppm in April 2016, while interannual variations exhibited an increasing trend of 2.28 ppm/a (Figure 3). The gray regions in Figure 3a represents the data unavailability in high latitudes during parts of the winter period. We de-trended the monthly average XCO₂ concentrations in order to investigate monthly variations in XCO₂ in China (Figure 3b). During the study period, XCO₂ concentrations reached a maximum in spring (Apr–May) and minimum in summer (Jul–Aug), with the average changes of XCO₂ amplitude reaching 6.78 ppm/a.

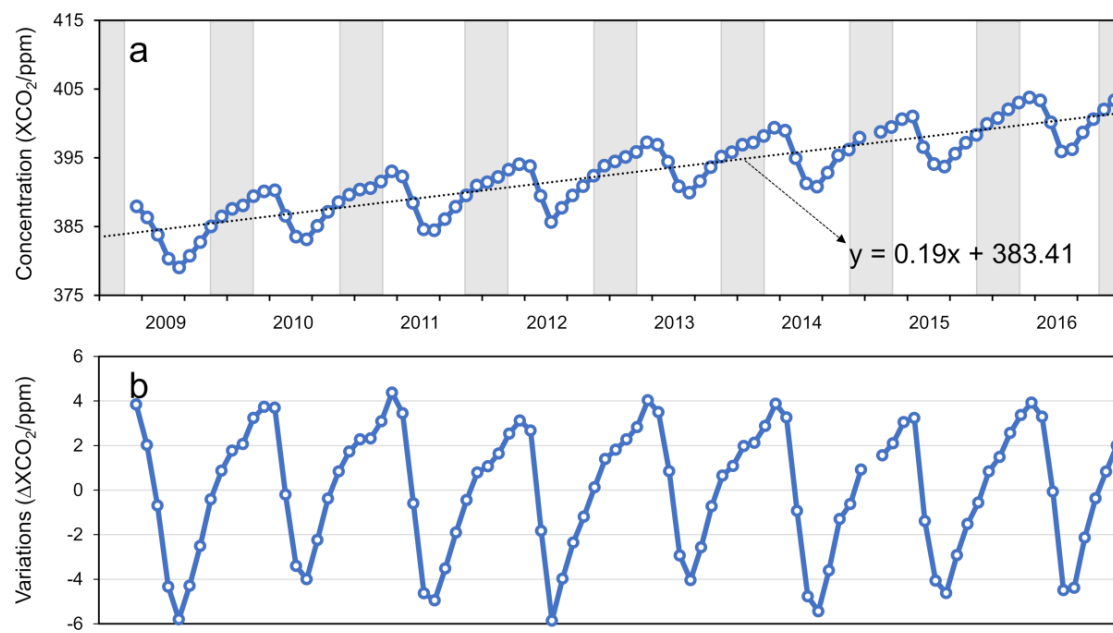


Figure 3. (a) Monthly changes and (b) detrended XCO₂ concentrations in China during 2009–2016 with gray indicating winter (data vacancy in January 2015).

Figure 4 illustrates the spatial characteristics of XCO₂ seasonal variation in China during 2009–2016. Maximum XCO₂ concentrations were observed in MAM (spring), while minimum values were detected for JJA (summer). More specifically, the derived XCO₂ concentrations from low to high were as follows: JJA (389.53 ppm) < SON (391.71 ppm) < DJF (394.37 ppm) < MAM (396.44 ppm). In particular,

the spatial distribution of atmospheric XCO₂ concentrations was observed to have drastically changed during summer, with concentrations decreasing rapidly with increasing latitude. China's low latitude coastal areas were associated with higher concentrations, while regions close to Mohe, Heilongjiang Province, exhibited low concentrations (only 387.00 ppm). In autumn, concentrations began to increase and the variance in spatial distribution was reduced. However, atmospheric XCO₂ concentrations in the densely populated areas of the North China Plain increased rapidly. In winter, atmospheric XCO₂ concentrations in eastern China continued to increase, widening the gap between the east and the west. The maximum concentration was observed close to the Henan and Shandong Provinces, while concentrations in the Ngari Prefecture and Qinghai–Tibet Plateaus were similar to those in spring (approximately 394.00 ppm).

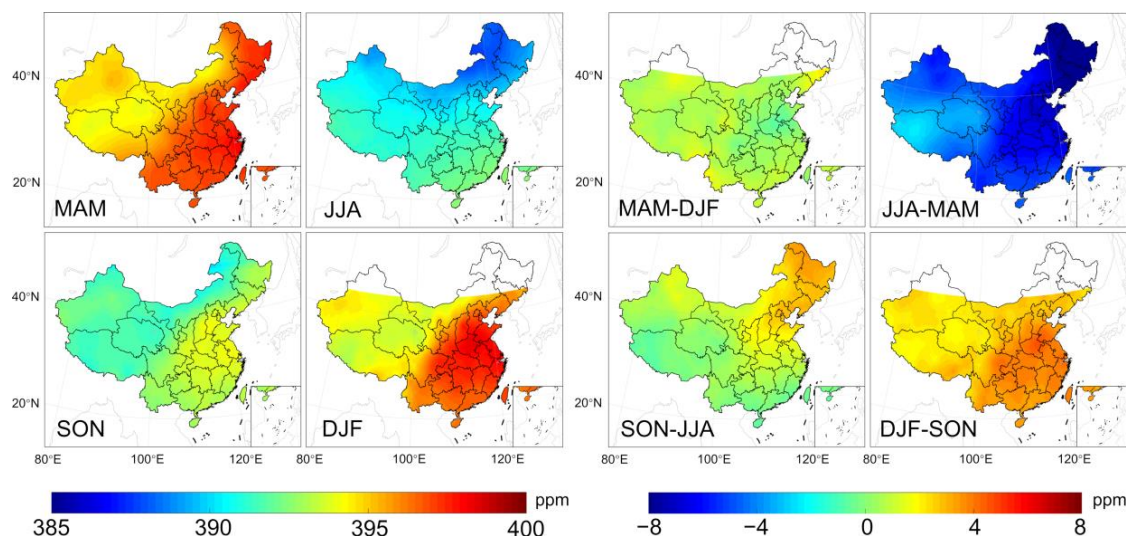


Figure 4. Seasonal averages of XCO₂ (ppm) from GOSAT over China during 2009–2016 and changes between seasons. MAM: March, April and May; JJA: June, July and August; SON: September, October and November; DJF: December, January and February.

In terms of spatial distribution, atmospheric XCO₂ concentrations dropped drastically from spring to summer, particularly in the three northeastern provinces, falling to −8.0 ppm (Figure 4). In addition, from summer to autumn, the concentrations in northeast and north China were observed to rise rapidly, with an increase of approximately 4.0 ppm. There was a slight increasing trend in concentrations in the western high latitude, while other parts of China exhibited relatively stable values. From autumn to winter, there was a visible growth in XCO₂ concentrations in China, particularly in the intersection of Shandong and Henan Provinces in the central and eastern parts of China, as well as in Chengdu and Chongqing. The growth rate of atmospheric XCO₂ slowed down from winter to spring, with most of China exhibiting a relatively stable trend. However, an increase of 1–2 ppm was observed in most parts of China. In addition, during this period, the concentration of atmosphere XCO₂ reached a maximum, with a multi-year average of 396.44 ppm.

3.3. Interannual Variations in XCO₂

Due to the temporal coverage of the GOSAT observation data, we focused on atmospheric XCO₂ concentrations during the vegetation growing season (GS, April–October each year). The area was divided into seven sub-regions based on seasonal variation characteristics (Figure 5), as also indicated by Wang et al. (2015) [14]. The sub-regions are as follows: (a) Northeast China (NEC), (b) North China (NC), (c) East China (EC), (d) Central China (CC), (e) South China (SC), (f) Northwest China (NWC) and (g) Southwest China (SWC). During the period from 2009 to 2016, the average XCO₂ concentrations

in sub-regions varied significantly (Table 2). Overall, the multi-year average concentration of XCO₂ in growing season reached 392.28 ppm in China.

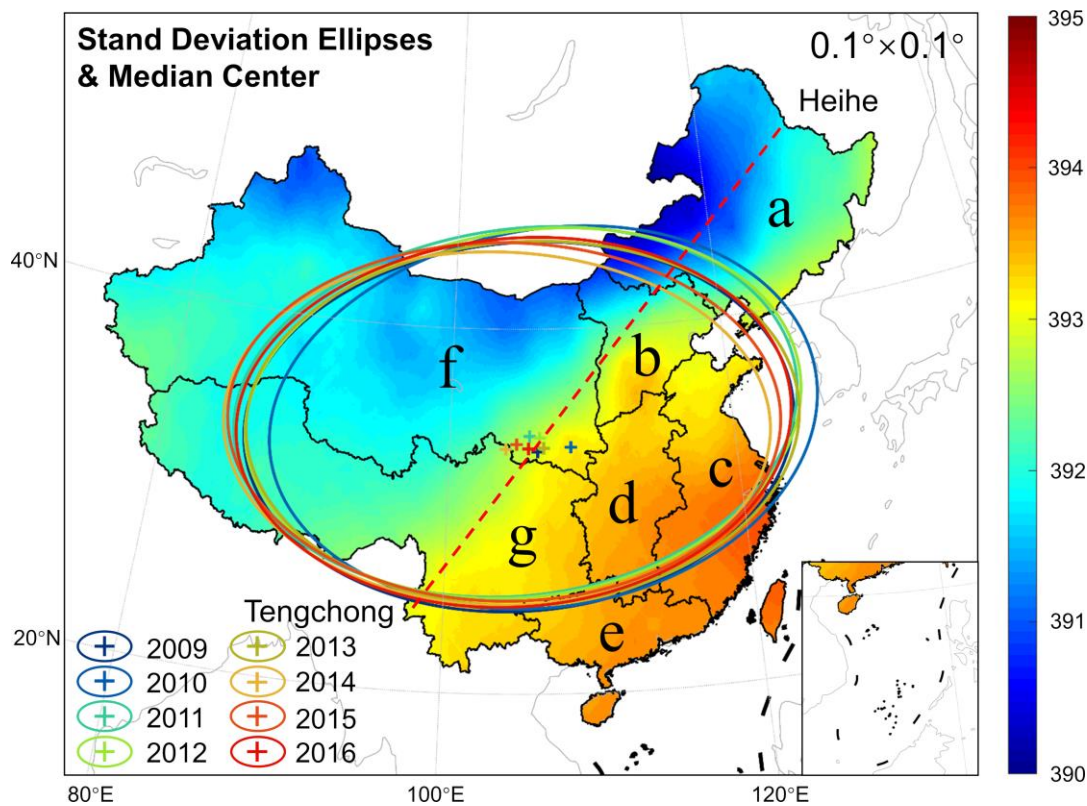


Figure 5. Average concentrations of XCO₂ (ppm) during the 2009–2016 growing seasons.

Table 2. Atmospheric XCO₂ concentrations (ppm) in the sub-regions during the 2009–2016 growing season.

	2009	2010	2011	2012	2013	2014	2015	2016	Mean
NEC	382.65	386.95	388.38	390.59	393.32	394.52	396.32	399.82	391.57
NC	383.71	387.43	388.72	391.35	394.66	395.59	397.85	400.95	392.53
CC	385.30	388.38	389.33	391.84	395.92	396.25	398.70	401.85	393.45
EC	385.36	388.26	389.48	391.91	395.90	396.48	399.03	402.04	393.56
SC	385.50	388.11	389.59	391.69	395.40	396.83	398.73	402.39	393.53
NWC	382.95	386.51	388.36	390.48	393.62	395.39	397.32	400.01	391.83
SWC	383.97	386.95	388.82	391.02	394.20	396.13	398.01	401.13	392.53
Mean	383.60	387.05	388.68	390.91	394.14	395.61	397.60	400.65	392.28
Var.	—	3.45	1.63	2.23	3.23	1.47	1.99	3.05	2.44

Figure 5 presents the general spatial pattern variations in annual XCO₂ concentrations for China in the growing seasons during 2009–2016 based on SDE analysis. The standard deviation ellipse represents the spatial distribution of most XCO₂ concentration in China. In particular, the major-axis indicates the extension direction of regions that exhibit high atmospheric XCO₂ concentrations. The minor-axis represents the distribution range of the high atmospheric XCO₂ concentration zone. In the growing seasons of 2009–2016; the major and minor axes of the ellipses covered regions from 19.31° to 20.13° and 9.96° to 10.10°, respectively. The ratios of the long semi-axis to the short half-axis were determined as 1.9239, 1.8831, 1.9998, 1.9785, 1.9686, 1.9950, 1.9958 and 1.9475, respectively. This indicates that the high concentration regions of atmospheric XCO₂ were generally located in east China, while the annual directions were relatively consistent and covered a stable range.

The median center represents the annual average center position of the entire atmospheric XCO₂ concentrations across China. The multi-year median centers of the atmospheric XCO₂ concentrations were observed to be evenly distributed to the left and right of the Hu line (red line in Figure 5). The average center of atmospheric XCO₂ concentrations in China is observed to have shifted north since the beginning of the study period. More specifically, between 2009 and 2016, the median center of atmospheric XCO₂ concentrations changed from 2009 (106.15° N, 33.27° E) to the easternmost point of 2010 (108.47° N, 33.50° E), and subsequently moved to the northernmost point of 2011 (105.59° N, 34.13° E). In 2011, the median center then began to slightly move to the 2009 median center. During 2011–2013, the 3-year average distance was determined as 83.43 km, with the 2014 median center located at the western zone of the country (103.93° N, 33.42° E). Finally, the median center moved east at a rate of approximately 69.09 km/a and ultimately returned to the 2009 location. The change in the median center indicates that the atmospheric XCO₂ concentration in China has a tendency to shift toward the northwestern part of China, except for special changes such as 2010.

However, the dispersion of atmospheric XCO₂ concentrations increased dramatically in 2010. This indicates that the proportion of atmospheric XCO₂ concentrations located in the northeastern direction of China suddenly increased significantly in 2010, with subsequent rates slowing from 2011 to 2013. In 2014, annual average concentrations in the southwestern region suddenly increased, dragging the median center to the southwest. Following this, concentrations slowed down in 2015 and 2016. Although two abnormal changes in atmospheric XCO₂ concentrations were observed across China in recent years, variations in concentrations remained relatively stable over the study period. In addition, the average center generally moved gradually to the northwest during the growing seasons of 2009–2016. Note that the average center extreme values of atmospheric XCO₂ concentrations in the northwest of Shaanxi Province in 2010 and in the southwest of Gansu Province in 2014 were 216.93 km away from the median center in 2009 and 245.49 km away from the median center in 2013, respectively. In addition, the azimuth angle of the standard deviation ellipse deflected 2.25° anticlockwise and 2.2° clockwise, respectively.

During the growing season, large differences were detected between the XCO₂ variations (Δ XCO₂) in sub-regions per year (Table 2). In China, the Δ XCO₂ values exhibited a gradual downward trend ($y = -0.04x + 2.61$) during the growing seasons of 2009–2016 (Figure 6). However, at high latitudes, the average Δ XCO₂ rates in NWC and NEC was rapidly reduced (-0.1 ppm/a). The second is North China, where the average Δ XCO₂ decreased at a rate of -0.05 ppm/a. Furthermore, Δ XCO₂ values in SWC were observed to fluctuate by 2–3 ppm/a, with relatively stable growth rates. However, in CC and EC, atmospheric XCO₂ levels exhibited a small upward trend ($+0.04$ ppm/a). The fastest annual growth trend was observed in SC, with the average Δ XCO₂ rate reaching $+0.19$ ppm/a and concentrations exhibiting an accelerated upward trend.

In 2010, variations in XCO₂ concentrations across China reached 3.45 ppm. However, east of Inner Mongolia, Heilongjiang Province, Jilin Province and Liaoning Province, values reached 4.22 ppm, 4.54 ppm, 4.63 ppm and 4.22 ppm, respectively. In particular, the increase of XCO₂ concentration in the Jilin Province was 142.9% of the national average. Furthermore, the average increase in NC also reached 3.7 ppm in 2010. In March 2010, the most severe continuous low temperature hazard since 1977 took place in northeastern China [52]. As a result, vegetation growth was slow in the spring of March–April, and thus NDVI values were only 59% of the multi-year average. This, in turn, affected atmospheric XCO₂ concentrations. Essentially, the large-scale and long-term persistence of low temperatures had a serious negative impact on the growth of vegetation in spring 2010, leading to restrictions in the ability of vegetation to absorb CO₂ from the atmosphere. Therefore, in 2010, the median center of China's atmospheric XCO₂ concentrations shifted in the northeast.

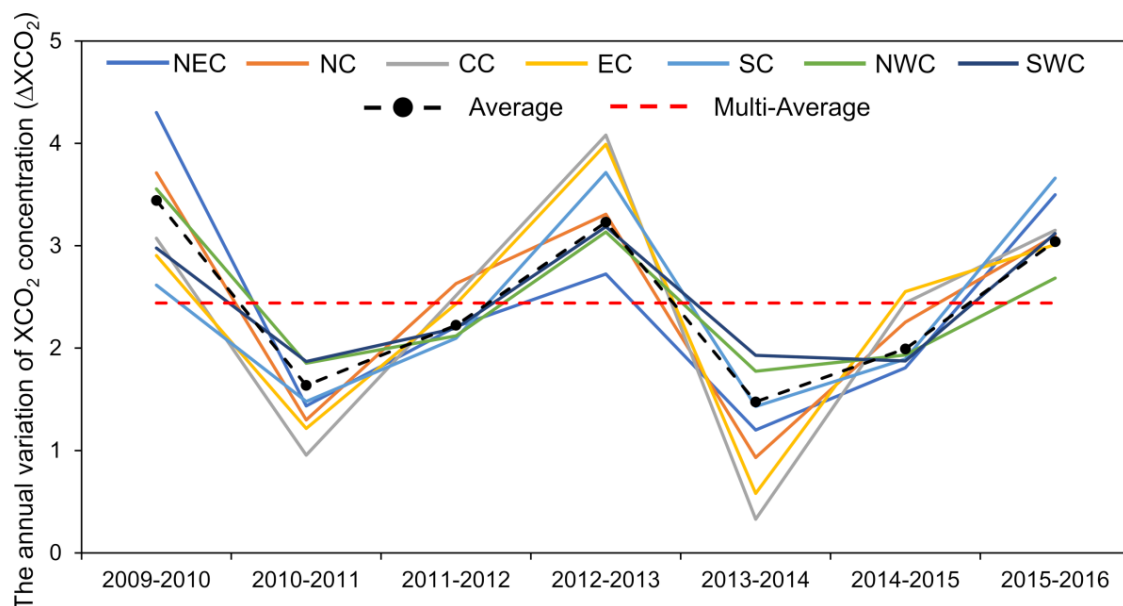


Figure 6. Variations of XCO₂ (ppm) in sub-regions during the 2009–2016 growing seasons.

In September 2013, China issued an action plan for the prevention and control of atmospheric pollution, which effectively controlled the production of high-energy consumption, high polluting and high emission enterprises in the Beijing–Tianjin–Hebei (BTH), Yangtze River Delta (YRD) and Pearl River Delta (PRD) regions. This was also an effective mitigation of atmospheric CO₂ emissions. According to the ODIAC CO₂ emissions dataset, fossil fuel combustion from human activities prior to 2013 exhibited a significant period of rapid growth (+0.13 g CO₂/m²/d), while the growth rate decreased significantly (+0.04 g CO₂/m²/d) following 2013. Furthermore, the most severe El Niño event since 2000 occurred in 2014–2016, which impacted precipitation and average temperatures in southeastern China. In particular, in 2015, precipitation in north China was reduced, with other parts of China experiencing severe drought. During the 2015/16 winter, average precipitation levels in south China (Guangdong, Guangxi and Hainan Provinces) reached historic values, exceeding those in perennial years by more than 1.6 times [53]. At the same time, the El Niño phenomenon also had a large impact on the variability of the atmosphere [54–56]. Thus, a series of related issues resulting from policy regulation and the El Niño phenomenon moved the median center of atmospheric XCO₂ concentrations to the east of China.

4. Discussion

4.1. Major Influencing Factors of XCO₂ in China

NDVI was generally observed as an important carbon sink affecting the long-term spatial distribution of atmospheric XCO₂ in China ($r = -0.83, p < 0.05$). This is consistent with results derived from SCIAMACHY data in China during 2003–2011 [14]. There was an obvious negative correlation belt from northeast to southwest China ($r < -0.75$), particularly in northeast China (Figure 7). This can control the absorption of carbon dioxide in the atmosphere through the photosynthesis of green vegetation [57,58]. Our results indicate that variations in atmospheric XCO₂ concentration were mainly affected by changes in vegetation cover. However, the effect of NDVI on XCO₂ concentrations varied spatially. In addition, a weak correlation ($r < 0.2$) was observed in the low latitudes of SWC and some areas of EC. Due to the low latitudes of Yunnan Province in the subtropical region, vegetation cover is present all year round. Consequently, the annual average NDVI was observed as 0.69; 176.9% of the national average. In eastern China, the vegetation growth was severely disturbed by anthropogenic activities. The majority of the agricultural waste formed by winter crops is incinerated in the open,

resulting in June NDVI values of only 57% of those in May and July. NWC compromises a large area of bare land with a monthly average NDVI of less than 0.25. Thus, in this region, the influence of vegetation on atmospheric XCO₂ concentrations is limited.

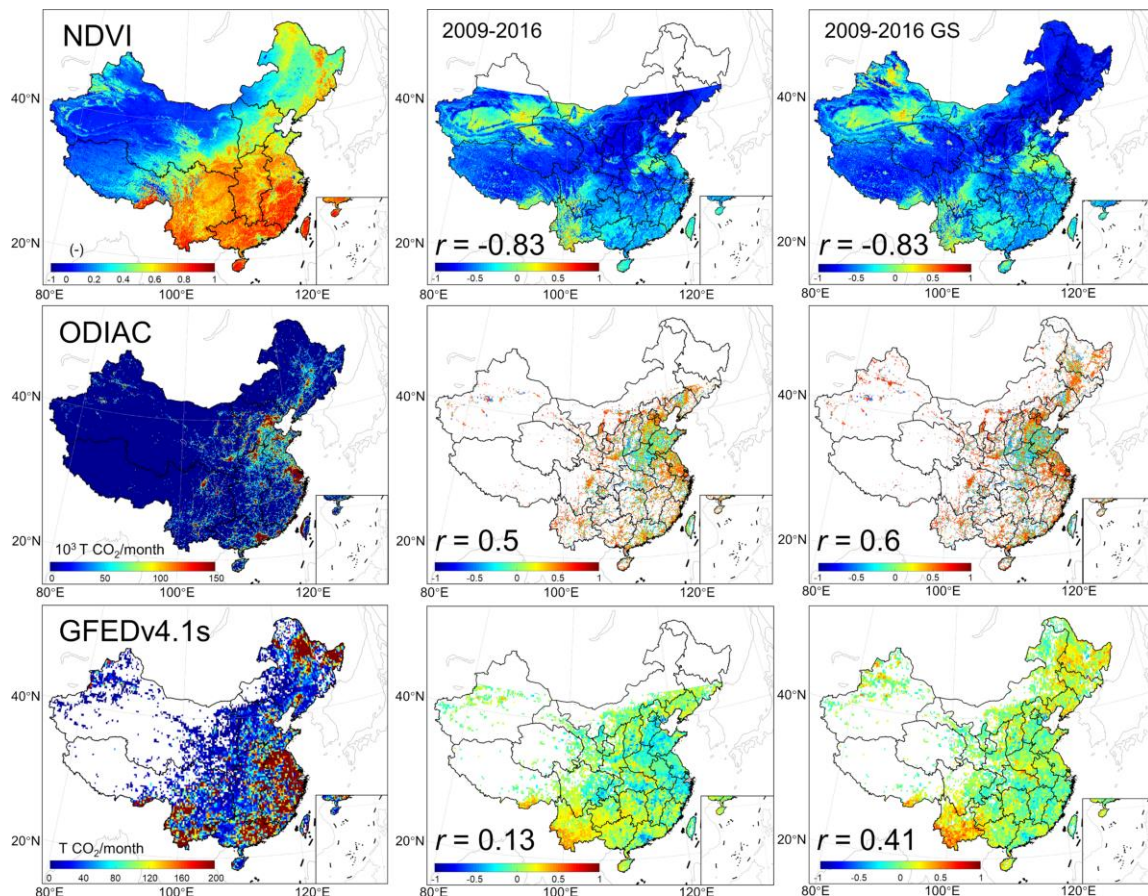


Figure 7. The correlation between XCO₂ and the driving factors in China during 2009–2016 (growing season, GS).

Emissions from human activity are the main contributors to CO₂ emissions [47,58]. As demonstrated in Figure 7 (ODIAC), most regions in China exhibited a highly positive correlation with the changes of XCO₂, particularly in the BTH, YRD, PRD and Sichuan–Chongqing economically developed areas. This shows that the intensity of human activity has an important impact on the spatial and temporal variation of XCO₂ concentrations. However, the correlation between the XCO₂ and Shandong and Henan Provinces, which have high population densities, were weak, whilst other regions in these two provinces exhibited negative correlations (Figure 7). This may be a result of the industrial structure and economic level of these regions. The CO₂ emissions from fossil fuel combustion in these two provinces (81.39 g CO₂/m²/day) was only 19.45% of those in Shanghai (418.38 g CO₂/m²/day).

Biomass burning emissions are a key source of atmospheric CO₂ [45,59]. Based on the biomass burning emission inventory (GFEDv4.1s) and derived CO₂ emissions in China (Figure 7), the annual average CO₂ emissions from biomass burning in China was determined as 76.9 Tg, with emissions distributed in Heilongjiang Province (14.4 Tg/a) and the three provinces along the southeastern coast (13.8 Tg/a). Yunnan Province in SWC (7.78 Tg/a) exhibited strong correlations with forest fires (55%) and the burning of savanna, grassland and shrublands (36.7%). The correlations of Heilongjiang Province in northeast China were slightly weak, yet the largest annual average emissions in China were associated with this region, and among them, agricultural straw waste burning was the main source of emissions (76.3% of total biomass burning emissions). In the eastern coastal areas, biomass combustion

emissions were more evident, and the main combustion type was agricultural waste combustion (51.5%). However, the correlation between biomass burning emission of this region with variations in atmospheric XCO₂ concentration was low ($r = 0.13$). In particular, in the eastern part of China, several areas exhibit negative correlations (Figure 7, GFED2009–2016). In addition, it has been observed that this area is also an area of high human activity (Figure 7, ODIAC). The same situation also occurred in the Pearl River Delta region, where human activity is strong in low and middle latitudes. Biomass burning emissions were greatly affected by human activity, and mainly occurred during spring. This spatial distribution trend determined here is similar to Qiu et al. [48].

The partial correlation and regression coefficients of the standardized multiple regression equations reveal the influence of the NDVI, ODIAC and GFED on atmospheric XCO₂ concentrations across different regions (Figure 8). NDVI (vegetation photosynthesis) had the greatest influence on the spatial pattern of atmospheric XCO₂ concentrations. Although photosynthesis plays a key role in various regions of China, its inhibition of XCO₂ concentrations is limited. Fossil fuel combustion, considered as the leading cause of the rapid growth in atmospheric XCO₂ concentrations in China, was the main carbon source of CO₂, particularly in medium and large cities (Figure 7). The regression coefficients almost reached 0.9 in sub-regions, with that of EC almost reaching 1.0. Biomass burning also contributed to XCO₂ concentrations in China, with contributions exhibiting significant regional heterogeneity, particularly in Yunnan Province in the southwest and Heilongjiang Province in the northeast (Figure 8b).

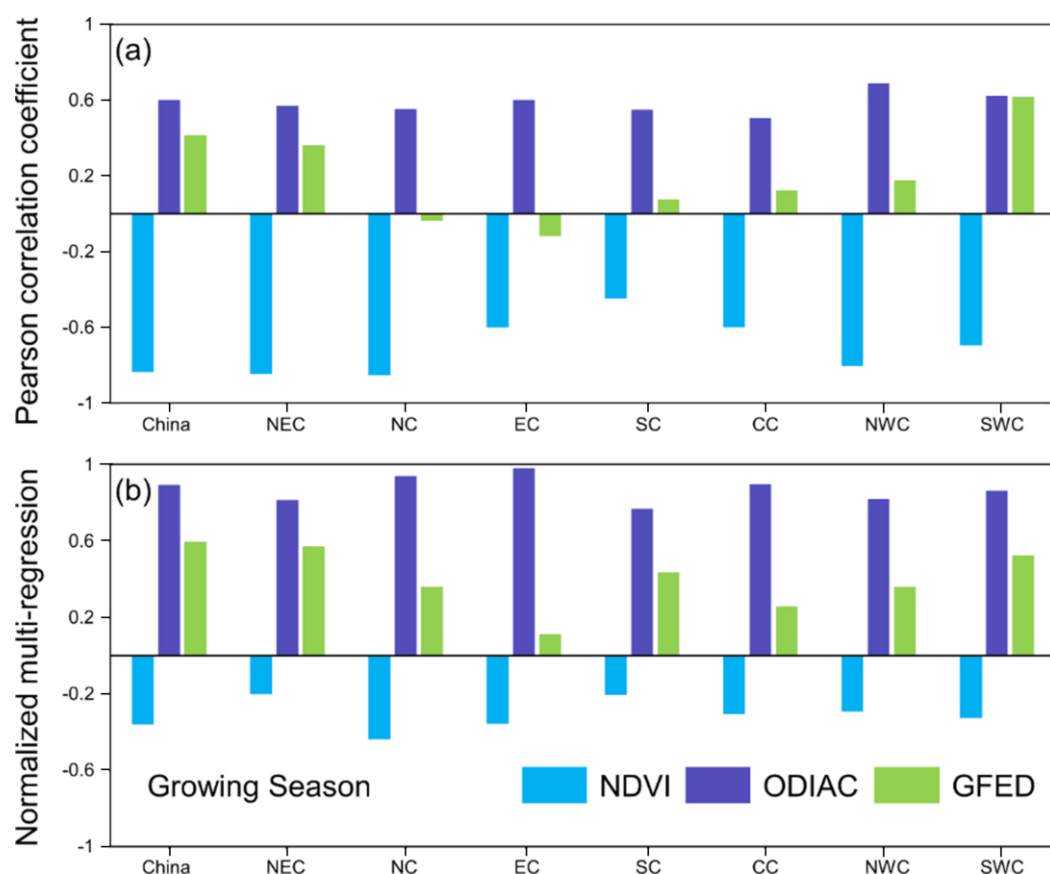


Figure 8. (a) Pearson correlation coefficients between the atmospheric XCO₂ concentrations, vegetation and emissions over China and other sub-regions. (b) Partial correlation coefficients between atmospheric XCO₂ concentrations and the three meteorological variables over China and sub-regions.

4.2. Contribution of XCO₂ in China

In summary, we used NDVI to represent carbon sinks, and human activities and fire emissions to represent carbon sources. We then quantified the effects of the fires, human activity and NDVI on the temporal changes in XCO₂ concentration per pixel during 2009–2016 (Figure 9). We found that NDVI dominated the whole study area, denoted by temporal XCO₂ variations, particularly in southwest and northwest China. A strong correlation was observed between NDVI and XCO₂, indicating that NDVI was the major influencing factor among the three factors in most parts of southwestern and northwestern China. However, the contribution rate of the three influencing factors in the other five regions exhibit significant seasonal variations, particularly in the east of Hu-line (red line in Figure 5). More specifically, the distribution of human activity and fire emissions were evaluated over the entire growing season. The areas where human activity (e.g., fossil fuel combustion) affected atmospheric XCO₂ concentrations were generally located in Shandong, Jiangsu and Henan Provinces, followed by Xi'an, Chengdu and Kunming. In the southeastern coastal areas and main inland urban areas, although fire emissions were high and human activity was intense, they were not focal influencing factors in these areas. Fire emissions predominantly occurred in Yunnan Province, and were also detected close to Henan Province and Chengdu.

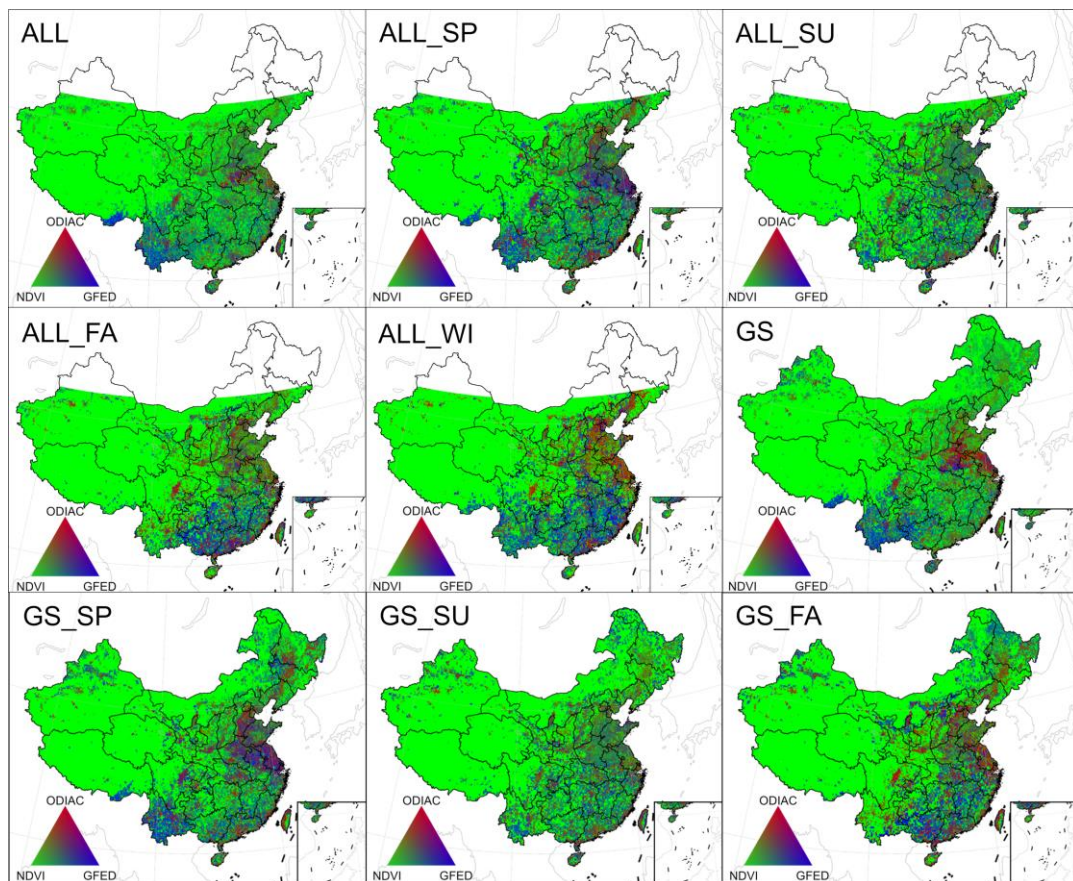


Figure 9. Contribution of each influencing factor during 2009–2016 (all months in study period, ALL, and growing season, GS).

The contribution of each factor varied across seasons. In spring, where vegetation respiration is stronger than photosynthesis, human activity and fire emissions contributed more to the atmospheric XCO₂ concentration, particularly in north and northeast China. In addition, fire emissions were principally detected in southeastern China, where a large continuous fire occurred in the north of eastern China, and a large number of sporadic fire spots appeared in southern China. In summer,

photosynthesis began to reach its maximum, and the impact of NDVI thus peaked. As a result, the atmospheric CO₂ concentration in China rapidly decreased to the lowest value, with an average of 389.53 ppm in this study period. These three main influencing factors did not show a clear dominant role in Yunnan Province and central East China. However, human activity still played an important role in major urban areas, particularly in the south-central region of China. In autumn, the impact of emissions from human activity was more evident, while the proportion of fire emissions in southeastern China also began to increase rapidly. Our results demonstrate that in east China, there was a large area affected by the three major driving factors. The shape of this area is similar to the equivalent area in spring and is also one of the most densely populated areas in China.

The contribution rate of each influencing factor experienced seasonal changes throughout 2009–2016. Throughout the study period, NDVI was a key factor in controlling atmospheric CO₂ concentration levels. The XCO₂ concentration in most areas of Henan Province, Chengdu and Kunming were affected by human activity; biomass burning emissions have a significant impact on CO₂ concentration levels in Yunnan Province. In terms of seasonal changes, the impact of human activity in spring at low latitudes rapidly increased, and the range of effects of biomass combustion on XCO₂ concentration increased. Furthermore, the contribution of biomass burning increased in southern China. In the winter, the impact of NDVI was further weakened. The emissions from biomass burning were concentrated in low latitudes below 25°N, particularly in Guangdong Province and Fujian Province. In addition to the impacts of NDVI, atmospheric XCO₂ concentrations were significantly affected by human activity. Fire emissions were observed to contribute to atmospheric XCO₂ concentrations, yet there were significant seasonal differences in the spatial distribution of its impacts.

5. Conclusions

In the current study, the seasonal cycle and inter-annual variations of XCO₂ over China based on a long-term (2009–2016) GOSAT dataset were analyzed. The main results can be summarized as follows.

(1) Atmospheric XCO₂ concentrations exhibited clear seasonal changes, with the highest concentrations observed in spring and the lowest in summer; (2) during 2009–2016, the average growth rate of XCO₂ concentration over China reached 2.28 ppm/a, and the average amplitude of seasonal variation was 6.78 ppm/a. In the growing season, the average XCO₂ concentration was determined as 392.28 ppm; (3) the regions with high XCO₂ concentrations were mostly distributed in southeast coastal areas, particularly the Yangtze River Delta region. In addition, low concentrations of XCO₂ were mainly observed in northern China; and (4) the contribution of each of the three driving factors exhibited significant spatial and temporal distribution heterogeneity. Atmospheric XCO₂ concentrations over China were mainly controlled by NDVI across time, with a significant negative correlation belt ($r < -0.75$) from northeast to southwest China. In addition, human activity was the main source of CO₂ emissions, and the biomass burning emissions also show an important impact on changes in atmospheric XCO₂ concentrations in northeast China in autumn and southwest China in spring.

The results of this study can provide us with a potential way to better understand the spatiotemporal changes of CO₂ concentration in China with NDVI, human activity and biomass burning, and could also have an enlightening effect on slowing the growth of CO₂ concentration in China. However, our study determined the relative contribution rates of the main influencing factors of CO₂, without quantifying the individual contributions of each factor. Therefore, a further study will focus on quantitatively attributing the effects of these factors, including the effects of atmospheric transport at various scales as well.

Author Contributions: Methodology, Y.S. and L.S.; project administration, Y.S. and S.Z.; writing—original draft, Z.L.; writing—review and editing, Y.S. All authors have read and agreed to the published version of the manuscript.

Funding: This research was supported by the National Key R&D Program of China, 2018YFB0504800 (2018YFB0504801). National Natural Science Foundation of China (41571199, 41701498), the Pioneer Hundred Talents Program of the Chinese Academy of Sciences (Y8YR2200QM), and NIES GOSAT-2 Project, Japan.

Acknowledgments: The authors sincerely thank the JAXA and NIES for providing the GOSAT data, and we would like to thank the NASA, WMO, GFED and ODIAC team for providing data support and sincerely appreciate the reviewers for their helpful comments to improve this manuscript.

Conflicts of Interest: The authors declare no conflict of interest.

References

1. Intergovernmental Panel on Climate Change. *Climate Change 2013: The Physical Science Basis. Contribution of Working Group I to the Fifth Assessment Report of the Intergovernmental Panel on Climate Change*; Cambridge University Press: Cambridge, UK, 2013; p. 1535.
2. Schneising, O.; Buchwitz, M.; Reuter, M.; Heymann, J.; Bovensmann, H.; Burrows, J.P. Long-term analysis of carbon dioxide and methane column-averaged mole fractions retrieved from SCIAMACHY. *Atmos. Chem. Phys.* **2011**, *11*, 2863–2880. [[CrossRef](#)]
3. World Data Centre for Greenhouse Gases. Available online: <https://gaw.kishou.go.jp/> (accessed on 1 February 2020).
4. Guan, D.; Peters, G.P.; Weber, C.; Hubacek, K. Journey to world top emitter: An analysis of the driving forces of China’s recent CO₂ emissions surge. *Geophys. Res. Lett.* **2009**, *36*, L04709. [[CrossRef](#)]
5. Cheng, S.; Zhou, L.; Tans, P.P.; An, X.; Liu, Y. Comparison of atmospheric CO₂, mole fractions and source–sink characteristics at four WMO/GAW stations in China. *Atmos. Environ.* **2018**, *180*, 216–225. [[CrossRef](#)]
6. Le Quéré, C.; Andrew, R.M.; Friedlingstein, P.; Sitch, S.; Pongratz, J.; Manning, A.; Korsbakken, J.I.; Peters, G.P.; Canadell, J.; Jackson, R.B.; et al. Global Carbon Budget 2017. *Earth Syst. Sci. Data Discuss.* **2018**, *10*, 405–448. [[CrossRef](#)]
7. Buermann, W.; Lintner, B.R.; Koven, C.; Angert, A.; Pinzon, J.E.; Tucker, C.J.; Fung, I.Y. The changing carbon cycle at Mauna Loa Observatory. *Proc. Natl. Acad. Sci. USA* **2007**, *104*, 4249–4254. [[CrossRef](#)] [[PubMed](#)]
8. Chevallier, F.; Deutscher, N.; Conway, T.J.; Ciais, P.; Ciattaglia, L.; Dohe, S.; Frohlich, M.; Gomez-Pelaez, A.J.; Griffith, D.; Hase, F.; et al. Global CO₂ fluxes inferred from surface air-sample measurements and from TCCON retrievals of the CO₂ total column. *Geophys. Res. Lett.* **2011**, *38*, L24810. [[CrossRef](#)]
9. Jing, Y.; Wang, T.; Zhang, P.; Chen, L.; Xu, N.; Ma, Y. Global Atmospheric CO₂ Concentrations Simulated by GEOS-Chem: Comparison with GOSAT, Carbon Tracker and Ground-Based Measurements. *Atmosphere* **2018**, *9*, 175. [[CrossRef](#)]
10. Heymann, J.; Reuter, M.; Buchwitz, M.; Schneising, O.; Bovensmann, H.; Burrows, J.P.; Massart, S.; Kaiser, J.; Crisp, D. CO₂ emission of Indonesian fires in 2015 estimated from satellite-derived atmospheric CO₂ concentrations. *Geophys. Res. Lett.* **2017**, *44*, 1537–1544. [[CrossRef](#)]
11. Buchwitz, M.; Reuter, M.; Schneising, O.; Noël, S.; Gier, B.; Bovensmann, H.; Burrows, J.P.; Boesch, H.; Anand, J.; Parker, R.J.; et al. Computation and analysis of atmospheric carbon dioxide annual mean growth rates from satellite observations during 2003–2016. *Atmos. Chem. Phys.* **2018**, *18*, 17355–17370. [[CrossRef](#)]
12. Reuter, M.; Bovensmann, H.; Buchwitz, M.; Burrows, J.P.; Connor, B.J.; Deutscher, N.; Griffith, D.W.T.; Heymann, J.; Keppel-Aleks, G.; Messerschmidt, J.; et al. Retrieval of atmospheric CO₂ with enhanced accuracy and precision from SCIAMACHY: Validation with FTS measurements and comparison with model results. *J. Geophys. Res. Atmos.* **2011**, *116*, D04301. [[CrossRef](#)]
13. Noël, S.; Bramstedt, K.; Hilker, M.; Liebing, P.; Plieninger, J.; Reuter, M.; Rozanov, A.; Sioris, C.; Bovensmann, H.; Burrows, J.P.; et al. Stratospheric, CH₄ and, CO₂ profiles derived from SCIAMACHY solar occultation measurements. *Atmos. Meas. Tech.* **2016**, *9*, 1485–1503. [[CrossRef](#)]
14. Wang, X.; Zhang, X.Y.; Zhang, L.Y.; Ling, G.; Lin, T. Interpreting seasonal changes of low-tropospheric CO₂, over China based on SCIAMACHY observations during 2003–2011. *Atmos. Environ.* **2015**, *103*, 180–187.
15. Jacob, D.; Turner, A.J.; Maasakkers, J.D.; Sheng, J.; Sun, K.; Liu, X.; Chance, K.; Aben, I.; McKeever, J.; Frankenberg, C. Satellite observations of atmospheric methane and their value for quantifying methane emissions. *Atmos. Chem. Phys.* **2016**, *16*, 14371–14396. [[CrossRef](#)]
16. Zeng, Z.-C.; Lei, L.; Strong, K.; Jones, D.B.A.; Guo, L.; Liu, M.; Deng, F.; Deutscher, N.; Dubey, M.K.; Griffith, D.W.T.; et al. Global land mapping of satellite-observed CO₂ total columns using spatio-temporal geostatistics. *Int. J. Digit. Earth* **2017**, *10*, 426–456. [[CrossRef](#)]

17. Jiang, X.; Crisp, D.; Olsen, E.; Kulawik, S.S.; Miller, C.E.; Pagano, T.; Liang, M.-C.; Yung, Y.L. CO₂ annual and semiannual cycles from multiple satellite retrievals and models. *Earth Space Sci.* **2016**, *3*, 78–87. [[CrossRef](#)]
18. De Kauwe, M.G.; Keenan, T.F.; Medlyn, B.E.; Prentice, I.C.; Terrer, C. Satellite based estimates underestimate the effect of CO₂ fertilization on net primary productivity. *Nat. Clim. Chang.* **2016**, *6*, 892–893. [[CrossRef](#)]
19. Yokota, T.; Yoshida, Y.; Eguchi, N.; Ota, Y.; Tanaka, T.; Watanabe, H.; Maksyutov, S. Global Concentrations of CO₂ and CH₄ Retrieved from GOSAT: First Preliminary Results. *SOLA* **2009**, *5*, 160–163. [[CrossRef](#)]
20. Turner, A.J.; Jacob, D.J.; Wecht, K.J.; Maasakkers, J.D.; Lundgren, E.; Andrews, A.E.; Biraud, S.C.; Boesch, H.; Bowman, K.W.; Deutscher, N.; et al. Estimating global and North American methane emissions with high spatial resolution using GOSAT satellite data. *Atmospheric Chem. Phys. Discuss.* **2015**, *15*, 7049–7069. [[CrossRef](#)]
21. Sheng, J.; Jacob, D.J.; Turner, A.J.; Maasakkers, J.D.; Benmergui, J.; Bloom, A.A.; Arndt, C.; Gautam, R.; Zavala-Araiza, D.; Boesch, H.; et al. 2010–2016 methane trends over Canada, the United States, and Mexico observed by the GOSAT satellite: contributions from different source sectors. *Atmospheric Chem. Phys. Discuss.* **2018**, *18*, 12257–12267. [[CrossRef](#)]
22. Kikuchi, N.; Yoshida, Y.; Uchino, O.; Morino, I.; Yokota, T. An advanced retrieval algorithm for greenhouse gases using polarization information measured by GOSAT TANSO-FTS SWIR I: Simulation study. *J. Geophys. Res. Atmos.* **2016**, *121*, 13129–13157. [[CrossRef](#)]
23. Makoto, I.; Isamu, M.; Osamu, U.; Nakatsuru, T.; Yoshida, Y.; Yokota, T.; Wunch, D.; Wennberg, P.; Roehl, C.M.; Griffith, D.W.T.; et al. Bias corrections of GOSAT SWIR XCO₂ and XCH₄ with TCCON data and their evaluation using aircraft measurement data. *Atmos. Meas. Tech.* **2016**, *9*, 3491–3512.
24. Guo, M.; Li, J.; Xu, J.; Wang, X.F.; He, H.S.; Wu, L. CO₂ emissions from the 2010 Russian wildfires using GOSAT data. *Environ. Pollut.* **2017**, *226*, 60–68. [[CrossRef](#)] [[PubMed](#)]
25. Basu, S.; Guerlet, S.; Butz, A.; Houweling, S.; Hasekamp, O.; Aben, I.; Krummel, P.B.; Steele, P.; Langenfelds, R.; Torn, M.S.; et al. Global CO₂ fluxes estimated from GOSAT retrievals of total column CO₂. *Atmospheric Chem. Phys. Discuss.* **2013**, *13*, 8695–8717. [[CrossRef](#)]
26. Wang, J.S.; Kawa, S.R.; Collatz, G.J.; Sasakawa, M.; Gatti, L.V.; Machida, T.; Liu, Y.; Manyin, M.E. A global synthesis inversion analysis of recent variability in CO₂ fluxes using GOSAT and in situ observations. *Atmospheric Chem. Phys. Discuss.* **2018**, *18*, 11097–11124. [[CrossRef](#)]
27. Tian, Y.; Sun, Y.; Liu, C.; Xie, P.; Chan, K.; Xu, J.; Wang, W.; Liu, J. Characterization of urban CO₂ column abundance with a portable low resolution spectrometer (PLRS): Comparisons with GOSAT and GEOS-Chem model data. *Sci. Total. Environ.* **2018**, *612*, 1593–1609. [[CrossRef](#)] [[PubMed](#)]
28. Detmers, R.G.; Hasekamp, O.; Aben, I.; Houweling, S.; Van Leeuwen, T.T.; Butz, A.; Landgraf, J.; Köhler, P.; Guanter, L.; Poulter, B. Anomalous carbon uptake in Australia as seen by GOSAT. *Geophys. Res. Lett.* **2015**, *42*, 8177–8184. [[CrossRef](#)]
29. Zhang, L.; Zhang, J. Analysis of the Seasonal Variation of CO₂ Concentration in China Based on GOSAT Satellite Data. *J. Indian Soc. Remote. Sens.* **2018**, *46*, 1667–1675. [[CrossRef](#)]
30. Houweling, S.; Baker, D.; Basu, S.; Boesch, H.; Butz, A.; Chevallier, F.; Deng, F.; Slugokenky, E.J.; Feng, L.; Ganshin, A.; et al. An intercomparison of inverse models for estimating sources and sinks of CO₂ using GOSAT measurements. *J. Geophys. Res. Atmos.* **2015**, *120*, 5253–5266. [[CrossRef](#)]
31. Alexe, M.; Bergamaschi, P.; Segers, A.; Detmers, R.; Butz, A.; Hasekamp, O.; Guerlet, S.; Parker, R.J.; Boesch, H.; Frankenberg, C.; et al. Inverse modelling of CH₄ emissions for 2010–2011 using different satellite retrieval products from GOSAT and SCIAMACHY. *Atmos. Chem. Phys.* **2015**, *15*, 113–133. [[CrossRef](#)]
32. Janardanan, R.; Maksyutov, S.; Oda, T.; Saito, M.; Kaiser, J.; Ganshin, A.; Stohl, A.; Matsunaga, T.; Yoshida, Y.; Yokota, T. Comparing GOSAT observations of localized CO₂ enhancements by large emitters with inventory-based estimates. *Geophys. Res. Lett.* **2016**, *43*, 3486–3493. [[CrossRef](#)]
33. Guo, M.; Xu, J.; Wang, X.; He, H.; Li, J.; Wu, L. Estimating CO₂ concentration during the growing season from MODIS and GOSAT in East Asia. *Int. J. Remote Sens.* **2015**, *36*, 4363–4383. [[CrossRef](#)]
34. Huang, X.; Wang, T.; Talbot, R.; Xie, M.; Mao, H.; Li, S.; Zhuang, B.; Yang, X.; Fu, C.; Zhu, J.; et al. Temporal characteristics of atmospheric CO₂ in urban Nanjing, China. *Atmos. Res.* **2015**, *153*, 437–450. [[CrossRef](#)]
35. Lei, L.; Zhong, H.; He, Z.; Cai, B.; Yang, S.; Wu, C.; Zeng, Z.; Liu, L.; Zhang, B. Assessment of atmospheric CO₂ concentration enhancement from anthropogenic emissions based on satellite observations. *Chin. Sci. Bull.* **2017**, *62*, 2941–2950. [[CrossRef](#)]

36. Bie, N.; Lei, L.; Zeng, Z.; Cai, B.; Yang, S.; He, Z.; Wu, C.; Nassar, R. Regional uncertainty of GOSAT XCO₂ retrievals in China: Quantification and attribution. *Atmos. Meas. Tech.* **2018**, *11*, 1251–1272. [[CrossRef](#)]
37. Liang, A.; Gong, W.; Han, G. Comparison of Satellite-Observed XCO₂ from GOSAT, OCO-2, and Ground-Based TCCON. *Remote Sens.* **2017**, *9*, 1033. [[CrossRef](#)]
38. Silva, S.; Arellano, A.; Worden, H. Toward anthropogenic combustion emission constraints from space-based analysis of urban CO₂/CO sensitivity. *Geophys. Res. Lett.* **2013**, *40*, 4971–4976. [[CrossRef](#)]
39. Mousavi, S.; Falahatkar, S.; Farajzadeh, M. Assessment of seasonal variations of carbon dioxide concentration in Iran using GOSAT data. *Nat. Resour. Forum* **2017**, *41*, 83–91. [[CrossRef](#)]
40. Shi, Y.; Matsunaga, T. Temporal comparison of global inventories of CO₂ emissions from biomass burning during 2002–2011 derived from remotely sensed data. *Environ. Sci. Pollut. Res.* **2017**, *24*, 16905–16916. [[CrossRef](#)]
41. Frankenberg, C.; Fisher, J.B.; Worden, J.; Badgley, G.; Saatchi, S.S.; Lee, J.E.; Toon, G.C.; Butz, A.; Jung, M.; Kuze, A.; et al. New global observations of the terrestrial carbon cycle from GOSAT: Patterns of plant fluorescence with gross primary productivity. *Geophys. Res. Lett.* **2011**, *38*, L17706. [[CrossRef](#)]
42. Parker, R.; Boesch, H.; Cogan, A.; Fraser, A.; Feng, L.; Palmer, P.I.; Messerschmidt, G.; Deutscher, N.; Griffith, D.W.T.; Notholt, J.; et al. Methane observations from the Greenhouse Gases Observing SATellite: Comparison to ground-based TCCON data and model calculations. *J. Geophys. Res. Atmos.* **2011**, *38*, L15807. [[CrossRef](#)]
43. Guo, M.; Wang, X.; Li, J.; Yi, K.; Zhong, G.; Tani, H. Assessment of Global Carbon Dioxide Concentration Using MODIS and GOSAT Data. *Sensors* **2012**, *12*, 16368–16389. [[CrossRef](#)] [[PubMed](#)]
44. Liu, D.; Lei, L.; Guo, L.; Zeng, Z.C. A Cluster of CO₂ Change Characteristics with GOSAT Observations for Viewing the Spatial Pattern of CO₂ Emission and Absorption. *Atmosphere* **2015**, *6*, 1695–1713. [[CrossRef](#)]
45. Shi, Y.; Matsunaga, T.; Noda, H. Interpreting Temporal Changes of Atmospheric CO₂ Over Fire Affected Regions Based on GOSAT Observations. *IEEE Geosci. Remote Sens. Lett.* **2017**, *14*, 77–81. [[CrossRef](#)]
46. Lim, C.; Kafatos, M.; Megonigal, P. Correlation between atmospheric CO₂ concentration and vegetation greenness in North America: CO₂ fertilization effect. *Clim. Res.* **2004**, *28*, 11–22. [[CrossRef](#)]
47. Oda, T.; Maksyutov, S. A very high-resolution (1 km × 1 km) global fossil fuel CO₂ emission inventory derived using a point source database and satellite observations of nighttime lights. *Atmos. Chem. Phys.* **2011**, *11*, 543–556. [[CrossRef](#)]
48. Qiu, X.; Duan, L.; Chai, F.; Wang, S.; Yu, Q.; Wang, S. Deriving High-Resolution Emission Inventory of Open Biomass Burning in China based on Satellite Observations. *Environ. Sci. Technol.* **2016**, *50*, 11779–11786. [[CrossRef](#)]
49. Giglio, L.; Randerson, J.T.; van der Werf, G.R. Analysis of daily, monthly, and annual burned area using the fourth-generation global fire emissions database (GFED4). *J. Geophys. Res. Biogeosci.* **2013**, *118*, 317–328. [[CrossRef](#)]
50. He, Q.; Gu, Y.; Zhang, M. Spatiotemporal patterns of aerosol optical depth throughout China from 2003 to 2016. *Sci. Total Environ.* **2019**, *653*, 23–35. [[CrossRef](#)]
51. Shi, Y.; Matsunaga, T.; Yamaguchi, Y.; Li, Z.; Gu, X.; Chen, X. Long-term trends and spatial patterns of PM 2.5 -induced premature mortality in South and Southeast Asia from 1999 to 2014. *Sci. Total Environ.* **2018**, *631–632*, 1504–1514. [[CrossRef](#)]
52. Wu, F. Studies on the Cause of Extreme Cold Temperature in Northeast China during March 2010 and Cold Surge, Ice-Snow and Frozen Disaster in South China during January 2008. Master’s Thesis, Ocean University of China, Qingdao, China, 2011.
53. Chen, J.; Wang, X.; Zhou, W.; Wang, C.; Xie, Q.; Li, G.; Chen, S. Unusual Rainfall in Southern China in Decaying August during Extreme El Niño 2015/16: Role of the Western Indian Ocean and North Tropical Atlantic SST. *J. Clim.* **2018**, *31*, 7019–7034. [[CrossRef](#)]
54. Zhai, P.; Yu, R.; Guo, Y. The Strong El Niño of 2015/16 and Its Dominant Impacts on Global and China’s Climate. *J. Meteorol. Res.* **2016**, *30*, 283–297. [[CrossRef](#)]
55. Yuan, Y.; Gao, H.; Jia, X.L.; Wan, J.H. Influences of the 2014–2016 Super El Niño Event on Climate. *Meteorol. Mon.* **2016**, *42*, 532–539.
56. Gong, H.; Wang, L.; Chen, W. Recently Strengthened Influence of ENSO on the Wintertime East Asian Surface Air Temperature. *Atmosphere* **2019**, *10*, 720. [[CrossRef](#)]

57. Rodrigues, C.P.; Fontana, D.C.; Moraes, O.L.L.D.; Roberti, D.R. NDVI and CO₂ flow in a soybean crop in Rio Grande do Sul, Brasil. *Rev. Bras. Meteorol.* **2013**, *28*, 95–104. [[CrossRef](#)]
58. Wei, N. Temporal and Spatial Distribution Characteristics of Atmospheric CO₂ Concentration in China Based on Satellite Remote Sensing and Its Influencing Factors. Master’s Thesis, East China Normal University, Shanghai, China, 2011.
59. Yang, Y.; Yu, Z. Quantification and evaluation of atmospheric pollutant emissions from open biomass burning with multiple methods: A case study for Yangtze River Delta region, China. *Atmos. Chem. Phys. Discuss.* **2019**, *19*, 327–348. [[CrossRef](#)]



© 2020 by the authors. Licensee MDPI, Basel, Switzerland. This article is an open access article distributed under the terms and conditions of the Creative Commons Attribution (CC BY) license (<http://creativecommons.org/licenses/by/4.0/>).